



Syngas production from methane and air via a redox process using Ce–Fe mixed oxides as oxygen carriers

Kongzhai Li, Hua Wang*, Yonggang Wei, Dongxia Yan

Faculty of Metallurgy and Energy Engineering, Kunming University of Science and Technology, Kunming 650093, China

ARTICLE INFO

Article history:

Received 22 October 2009

Received in revised form 6 April 2010

Accepted 16 April 2010

Available online 22 April 2010

Keywords:

Methane selective oxidation

Syngas

Gas–solid reaction

Ce–Fe solid solution

Surface Fe species

ABSTRACT

CeO₂, Fe₂O₃, Fe₂O₃/Al₂O₃ and Ce–Fe mixed oxides with different Ce/Fe ratios were prepared and characterized using XRD, Raman, XPS, and H₂–TPR techniques. The selective oxidation of methane to syngas using a gas–solid reaction was investigated at 850 °C. For binary Ce–Fe oxides, only small amounts of iron ions could be incorporated into the CeO₂ lattice with the superfluous Fe₂O₃ remaining on the surface of the molecule. Chemical interactions between surface iron sites and the Ce–Fe solid solution strongly enhanced the reducibility of materials. Methane was found to adsorb and activate on the surface iron sites as carbonaceous species and hydrogen. Carbon deposition was selectively oxidized to CO by the release of activated oxygen from the CeO₂ lattice. The activation rate of methane was dependent on the quality of dispersion of surface Fe species, while the oxygen mobility of the material dominated the CO formation rate. Hydrothermally prepared Ce_{0.7}Fe_{0.3}O_{2–δ} showed high activity and selectivity during the successive production of syngas using repetitive redox processes (methane reduction/air re-oxidation). Both the dispersion of surface Fe₂O₃ and the formation of the Ce–Fe solid solution were enhanced by the redox treatment, which made the oxygen carrier more stable.

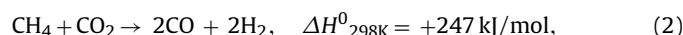
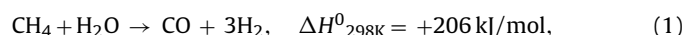
Crown copyright © 2010 Published by Elsevier B.V. All rights reserved.

1. Introduction

Methane, the main component of natural gas and coal-bed gas, is also a byproduct of the decay or fermentation of organic materials. Because methane has great potential as an energy source its conversion to more useful and easily transportable chemicals may contribute to the creation of carbon-neutral energy chains in the future [1]. Commercial processes in methane conversion such as gas-to-liquids (GTLs), methanol synthesis and hydrogen generation from water gas shift (WGS) are all based on a mixture of H₂ and CO commonly referred to as syngas [2,3]. It is estimated that syngas generation accounts for more than half the capital investment and a disproportionate share of the operating cost in these processes [4,5].

Steam methane reforming (SMR), carbon dioxide reforming (CDR) and partial oxidation of methane (POM) represent three principal routes for syngas generation from methane [6]. Both SMR and CDR are highly endothermic as shown in Eqs. (1) and (2). By contrast, POM is mildly exothermic with a H₂/CO ratio of about 2.0 (Eq. (3)), which makes it suitable for methanol production or

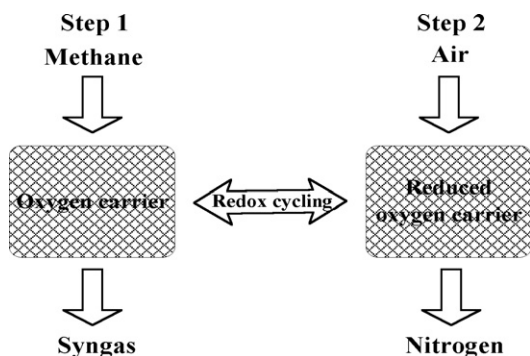
Fischer–Tropsch synthesis. Since the rate of an oxidation reaction is very fast, it also allows small reactors and a high throughput [3]. However, the direct oxidation process has not been used commercially given the high-temperature gradients, the risk of explosion of premixed CH₄/O₂ mixtures, and the expense of supplying pure oxygen [7]:



To avoid these problems, Van Looij et al. [8] and Otsuka et al. [9] proposed a novel two-step method for synthesis gas production using the lattice oxygen of metal oxides during gas–solid reactions. In the process of Van Looij, methane (in the absence of gas-phase oxygen) is first oxidized to CO₂ and H₂O using an oxygen carrier. This is followed by reforming of methane to produce CO and H₂, and finally the lower valent oxide or metal is regenerated by air [7,8]. High temperatures (>800 °C) and additional catalysts such as Ni/Al₂O₃ are required to accomplish endothermic reforming process. In Otsuka's findings, methane reacted directly with a suitable oxygen carrier to produce H₂ and CO after which the reduced oxygen carrier was re-oxidized by CO₂ or H₂O to obtain pure CO or H₂ [9,10]. Although CeO₂ and a CeO₂–ZrO₂ solid solution were used in this process, the reduced CeO₂ or CeO₂–ZrO₂ mixed oxides could not be recovered completely by CO₂ or H₂O [10–12]. The direct

* Corresponding author at: Room 217, Faculty of Metallurgy and Energy Engineering, Kunming University of Science and Technology, Kunming 650093, China. Tel.: +86 871 5153405; fax: +86 871 5153405.

E-mail address: wanghuaheat@hotmail.com (H. Wang).



Scheme 1. Schematic of the direct conversion of methane to synthesis gas by means of gas–solid reactions.

selective oxidation of methane by suitable oxygen carriers followed by their re-oxidation by air (see Scheme 1) seems to be a more viable option [13–18]. Air is used instead of pure oxygen allowing considerable cost savings and the separation of fuel from the gaseous oxidant avoids the risk of explosion.

CeO₂ is one of the most attractive oxides in the catalytic and material fields because oxygen vacancy defects can be rapidly formed and eliminated over a wide range of working temperatures, which allows high “oxygen storage capacity (OSC)” [19,20]. Some ceria-based materials (e.g., CeO₂ promoted by Pt, Ce–Zr–O and Ce–Sm–O systems) have shown high selectivity for syngas production using a two-step method, but have had relatively low efficiency [9–13,16,21]. Trivalent ions in ceria lower the activation energy required for oxygen migration, while the addition of smaller ions enhances OSC by creating oxygen defects and delaying OSC degradation at high temperatures [22–25]. Doped-ceria with undersized lower valence ions such as Fe³⁺ have shown enhanced oxidation activity and catalytic properties through the formation of surface structural defects and a ceria-like solid solution [25–28]. In addition, modified iron oxides have also been used as oxygen carriers to produce CO and H₂ via methane [18,29]. In previous researches of our team, Ce–Fe mixed oxides with a Ce/Fe ratio higher than 1:1 showed high activity and selectivity during the selective oxidation of methane to synthesis gas by gas–solid reactions [30,31]. However, the detailed information on the methane selective oxidation using Ce–Fe mixed oxides as oxygen carriers, especially on the structure–activity relationship and reaction mechanism, has not been obtained.

The present work investigates the structure characteristic and reactivity of Ce–Fe materials. Special attention is given to interactions between dispersed iron sites and the Ce–Fe solid solution. Cyclic experiments (methane reduction/air re-oxidation) for the successive production of syngas and the performance optimization of oxygen carriers were also performed. Discussion of a possible reaction mechanism is based on the results.

2. Experimental

2.1. Oxygen carrier preparation

Ce_{1-x}Fe_xO_{2-δ} ($x=0, 0.1, 0.2, 0.3, 0.4, 0.5, 1$) mixed oxide series were prepared by co-precipitation. The required amounts of Ce(NO₃)₃·6H₂O and/or Fe(NO₃)₃·9H₂O were dissolved in deionized water, blended using a magnetic stirrer and heated to 70 °C. The hydroxides were precipitated by dropping an ammonia solution. The mixtures were stirred for one hour, when their pH increased to 8 and 10. The precipitates were dried at 110 °C for 24 h, subjected to decomposition at 300 °C for 2 h, then ground to powders and calcinated under ambient air at 800 °C for 6 h. The Fe₂O₃/Al₂O₃

(Al/Fe=7:3) mixed oxides were similarly prepared. The starting materials were Fe(NO₃)₃·9H₂O and Al(NO₃)₃·9H₂O.

Pure CeO₂ and Fe₂O₃ powders were used for the preparation of the Ce_{0.7}Fe_{0.3}O_{2-δ} sample by solid phase syntheses. The blended powders (CeO₂ and Fe₂O₃) were finely ground before calcination under ambient air at 800 °C for 6 h.

The hydrothermal methodology was as reported in [24]. The required amounts of Ce(NO₃)₃·6H₂O and Fe(NO₃)₃·9H₂O (Ce/Fe = 7:3) were dissolved in deionized water and well mixed. The total concentration of Ce and Fe nitrate was 0.25 mol/L. A brown slurry was precipitated by gradually dripping in an ammonia solution while maintaining the pH at about 10 with stirring. Then, 65 cm³ of slurry was transferred to 100 cm³ Teflon-lined stainless steel autoclaves and reacted at 220 °C for 48 h. After cooling, the sample was washed with distilled water and ethanol three times before air-drying at 110 °C for 12 h.

2.2. Oxygen carrier characterization

X-ray diffraction (XRD) was performed on a Japan Science D/max-R diffractometer using Cu Kα radiation ($\lambda=0.15406$ nm). The X-ray tube was operated at 40 kV and 40 mA. The X-ray diffractogram was recorded at 0.01° intervals with a scanning rate of 5°/min for the scanning angle (2θ) from 10° to 80° and of 0.5°/min for the 2θ from 27.5° to 29.5°, respectively.

Temperature-programmed reduction (TPR) experiments were performed on a TPR Win v 1.50 (produced by Quantachrome Instruments Co.) under a 10% H₂/He mixture (75 mL/min) flow using 100 mg catalysts at a heating rate of 10 °C/min.

The Raman spectrum of oxygen carriers was recorded in a Renishaw Invia Raman imaging microscope. The exciting wavelength from an Ar ion laser with a power of 4 mW on the samples was 514.5 nm. The scanning range was set between 100 and 1800 cm⁻¹.

The X-ray photoelectron spectroscopy (XPS) experiments were carried out on a PHI-5500 system equipped with a monochromatic Mg Kα X-rays source ($h\nu=1253.6$ eV). Spectra were registered after purging the samples at ambient temperature in a vacuum (residual pressure < 10⁻⁷ Pa). An electron flood gun compensated sample charging during the measurement. The electron takeoff angle was 45° with respect to the sample surface. The spectra were referenced to the C 1s emission at 284.8 eV.

Specific surface area of oxygen carrier was calculated according to the BET method by the N₂ adsorption isotherm at -196 °C, using a Quantachrome NOVA 2000e instrument.

2.3. Catalytic activity tests

Reactions: the selective oxidation of CH₄ was carried out in a fixed-bed reactor system under atmospheric pressure. An oxygen carrier (1.0 g) was placed in a quartz tube with 19 mm inside diameter. Prior to catalytic reactions, the oxygen carriers were heated in air at 200 °C for 2 h, and then pure N₂ flowed through the reactor for one hour at 300 °C. The reactions between methane (99.99% purity) and Ce–Fe oxygen carriers were performed at 850 °C and the gas flow rate of methane was controlled at 10 mL/min. Reactant and product components were analyzed by a gas chromatograph (GC112A, produced by Shanghai Precision & Scientific instrument Co.) equipped with a thermal conductivity detector (TCD). Argon was used as the carrier gas.

The CH₄ conversion and CO or H₂ selectivity were calculated as follows:

$$\text{methane conversion (\%)} = \frac{\text{moles of methane consumed}}{\text{moles of methane introduced}} \times 100$$

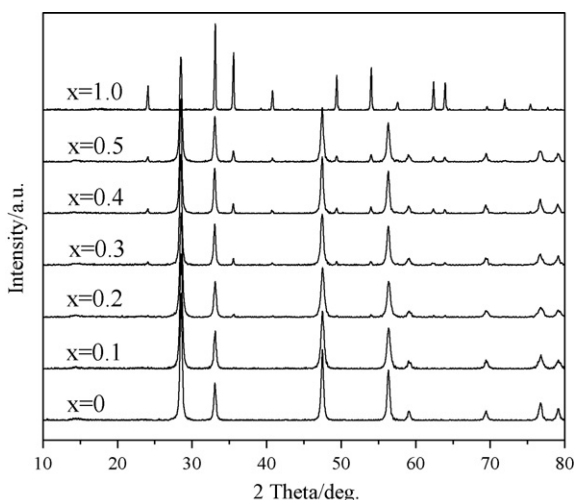


Fig. 1. XRD patterns of $\text{Ce}_{1-x}\text{Fe}_x\text{O}_{2-\delta}$ oxygen carriers ($x = 0, 0.1, 0.2, 0.3, 0.4, 0.5$, and 1).

$$\text{CO selectivity (\%)} = \frac{\text{moles of CO produced}}{\text{total moles of CO and CO}_2 \text{ produced}} \times 100$$

$$\text{H}_2 \text{ selectivity (\%)} = \frac{\text{moles of H}_2 \text{ produced}}{\text{moles of methane introduced} \times 2} \times 100$$

Successive redox cycles: after the reaction between methane (10 mL/min) and the oxygen carrier (1.0 g) had proceeded for 10 min (reducing step), compressed air was introduced at 60 mL/min for 16 min to regenerate the reduced sample (re-oxidation step). These sequences were separated by a purge of pure N_2 (80 mL/min) for 10 min to avoid mixing the gases arising during the two steps. The reaction temperature in the whole process was maintained at 850 °C.

3. Results and discussion

3.1. XRD patterns

Fig. 1 shows the XRD patterns of the $\text{Ce}_{1-x}\text{Fe}_x\text{O}_{2-\delta}$ oxygen carriers prepared by co-precipitation. The CeO_2 diffractogram was characteristic of a cubic fluorite-structured material [11] with all the diffraction peaks for pure Fe_2O_3 attributed to $\alpha\text{-Fe}_2\text{O}_3$ [32]. The $\text{Ce}_{0.9}\text{Fe}_{0.1}\text{O}_{2-\delta}$ sample only displayed reflections from CeO_2 without the characteristic Fe_2O_3 peaks. Very weak $\alpha\text{-Fe}_2\text{O}_3$ characteristic peaks appeared in $\text{Ce}_{0.8}\text{Fe}_{0.2}\text{O}_{2-\delta}$ sample and intensified with increases in iron content. Table 1 shows the lattice constant for ceria decreases with the further addition of iron ions (0.542, 0.540

and 0.539 nm for pure CeO_2 , $\text{Ce}_{0.9}\text{Fe}_{0.1}\text{O}_{2-\delta}$ and $\text{Ce}_{0.8}\text{Fe}_{0.2}\text{O}_{2-\delta}$, respectively). This lattice contraction is due to the incorporation of smaller Fe^{3+} into the lattice of CeO_2 , evidencing the formation of a Ce–Fe solid solution [25,28]. However, the CeO_2 lattice constant returned to that of pure CeO_2 with further increases in iron content (Table 1). This suggests that iron content beyond a limit would prevent solid solution formation and thus supporting the proposition that iron ions is extremely difficult to dissolve into the ceria lattice and that the dopant content is limited to ca. 15% [24]. As a consequence, only the $\text{Ce}_{0.9}\text{Fe}_{0.1}\text{O}_{2-\delta}$ sample presented a complete solid solution, while $\text{Ce}_{0.8}\text{Fe}_{0.2}\text{O}_{2-\delta}$ and $\text{Ce}_{0.7}\text{Fe}_{0.3}\text{O}_{2-\delta}$ samples revealed the co-existence of crystallized Fe_2O_3 and Ce–Fe solid solutions. $\text{Ce}_{0.6}\text{Fe}_{0.4}\text{O}_{2-\delta}$ and $\text{Ce}_{0.5}\text{Fe}_{0.5}\text{O}_{2-\delta}$, on the other hand, exhibited segregated Fe_2O_3 and CeO_2 phases. The lattice constants for $\alpha\text{-Fe}_2\text{O}_3$ in the entire Ce–Fe mixed oxides were similar with that of the pure Fe_2O_3 sample, indicating that the structure of Fe_2O_3 was not affected by the presence of CeO_2 .

The average crystallite sizes of CeO_2 , as calculated using Scherrer equation, are also reported in Table 1, with 23 nm for the pure CeO_2 sample and decreasing to less than 20 nm for $\text{Ce}_{0.9}\text{Fe}_{0.1}\text{O}_{2-\delta}$, $\text{Ce}_{0.8}\text{Fe}_{0.2}\text{O}_{2-\delta}$ or $\text{Ce}_{0.7}\text{Fe}_{0.3}\text{O}_{2-\delta}$ samples. This decline is characteristic of materials with greater thermal stability due to the formation of solid solution [33].

3.2. Reducibility (TPR)

The reducibility of Ce–Fe oxygen carriers were investigated using H_2 –TPR measurement (Fig. 2). The hydrogen reduction profile for Fe_2O_3 is generally accepted to be stepwise [32], with Fe_2O_3 first converting to Fe_3O_4 and then to Fe. Two sequential reduction peaks (at ca. 635 °C and above 670 °C) were observed for pure Fe_2O_3 and should correspond to the above two reduction processes. The reduction of pure CeO_2 is evidenced by three peaks at ca. 145, 340 and above 900 °C and should correspond to the sequential reductions of adsorption oxygen, surface lattice oxygen and bulk oxygen [34]. The $\text{Ce}_{1-x}\text{Fe}_x\text{O}_{2-\delta}$ binary oxides ($x = 0.1, 0.2, 0.3, 0.4, 0.5$) also presented three reduction peaks, labeled α , β and γ , with increases in temperature. The reduction of $\text{Ce}_{0.9}\text{Fe}_{0.1}\text{O}_{2-\delta}$ must be related to the consumption of oxygen in surface and bulk of ceria-like solid solution. In the other Ce–Fe samples, the intensity of the α peak gradually strengthened with increased iron content (corresponding to the increased XRD peaks for the Fe_2O_3 in Fig. 1) and suggesting that this peak should be attributed to the reduction of Fe^{3+} located on the surface. Identifying the origin of the β and γ reduction peaks was not easy because of possible peak overlaps caused by the simultaneous reduction of Fe^{2+} and Ce^{4+} . Note that the intensity of the β and γ peaks decreased when the iron content further increased

Table 1

Structural characteristics of $\text{Ce}_{1-x}\text{Fe}_x\text{O}_{2-\delta}$ oxygen carriers ($x = 0, 0.1, 0.2, 0.3, 0.4, 0.5$, and 1).

Oxygen carriers	Crystallite size (nm) CeO_2	Lattice constant (nm)		
		CeO_2		
		a	a	c
CeO_2	23	0.542	–	–
Fe_2O_3	–	–	0.505	1.380
$\text{Ce}_{0.9}\text{Fe}_{0.1}\text{O}_{2-\delta}$	17	0.540	–	–
$\text{Ce}_{0.8}\text{Fe}_{0.2}\text{O}_{2-\delta}$	16	0.539	0.504	1.380
$\text{Ce}_{0.7}\text{Fe}_{0.3}\text{O}_{2-\delta}$	19	0.539	0.505	1.380
$\text{Ce}_{0.6}\text{Fe}_{0.4}\text{O}_{2-\delta}$	21	0.541	0.505	1.381
$\text{Ce}_{0.5}\text{Fe}_{0.5}\text{O}_{2-\delta}$	21	0.541	0.505	1.381

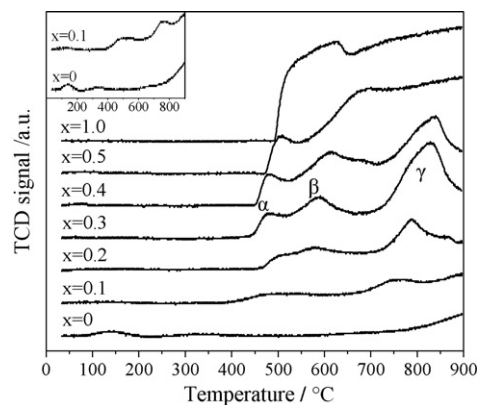


Fig. 2. H_2 –TPR profiles of $\text{Ce}_{1-x}\text{Fe}_x\text{O}_{2-\delta}$ oxygen carriers ($x = 0, 0.1, 0.2, 0.3, 0.4, 0.5$, and 1).

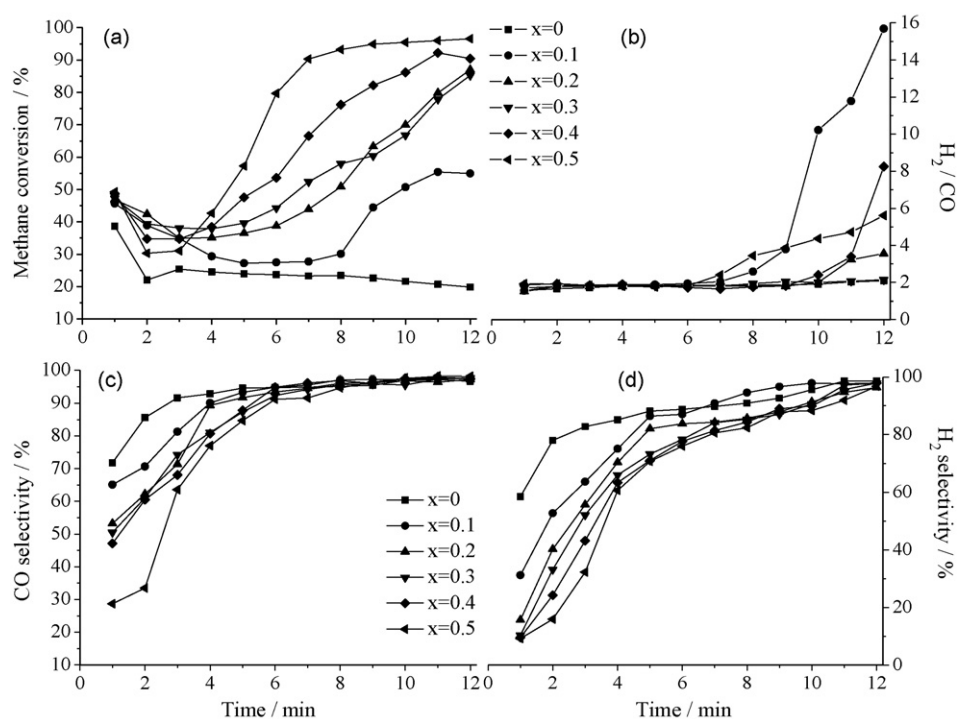


Fig. 3. CH₄ conversion (a), H₂/CO ratio (b), CO selectivity (c) and H₂ selectivity (d) vs. reaction time over Ce_{1-x}Fe_xO_{2-δ} oxygen carriers (x=0, 0.1, 0.2, 0.3, 0.4, and 0.5).

from 30% (x=0.3) to 40% (x=0.4). The patterns for these two peaks in the Ce_{0.5}Fe_{0.5}O_{2-δ} sample were both hard to distinguish and similar to those for pure Fe₂O₃. This would suggest that the above two peaks may be attributed to the reduction in surface and bulk CeO₂, and that the overlapping reduction of Fe²⁺ to Fe also contributed to the process, especially for samples with a relatively high iron content.

Generally, the generation of oxygen vacancies leads to an easy release of oxygen. However, even Ce_{0.6}Fe_{0.4}O_{2-δ} with no solid solution is also easily reduced than a pure CeO₂. The chemical interaction between free Fe species and CeO₂ seems to play an important role during the reduction of Ce–Fe materials. As a consequence, the Ce_{0.7}Fe_{0.3}O_{2-δ} sample with a coexisting solid solution and free Fe₂O₃ particles showed the best redox property. It is similar with the observation that an interaction between surface NiO and Ce–Ni solid solution strongly enhanced the reducibility of materials [35].

3.3. Gas–solid reaction between CH₄ and Ce_{1-x}Fe_xO_{2-δ}

In an earlier work on temperature-programmed reactions between methane and Ce_{1-x}Fe_xO_{2-δ} oxygen carriers, our results suggested that the selective oxidation of methane would be highly efficient at high temperatures (e.g., 850 °C) [30,36]. Fig. 3 shows typical kinetic curves for methane conversion, CO and H₂ selectivity, and the H₂/CO ratio in the reaction of CH₄ with Ce_{1-x}Fe_xO_{2-δ} at 850 °C. The average data during these reactions are shown in Table 2.

As seen in Fig. 3(a), methane conversion was relatively high in the initial stage but decreased sharply later, after which a rapid increase for Ce–Fe samples and a slow decline for pure CeO₂ were observed. The selectivity of CO and H₂ increased quickly and reached a relative steady state (Fig. 3(c) and (d)). Table 2 shows that CeO₂ presented the highest selectivity but also the lowest conversion. Although higher iron content produced greater methane conversion, there was relatively lower syngas selectivity. This suggests that Fe species may be the active sites for methane activation and that CeO₂ can provide the necessary oxygen for syngas generation.

Generally, there are two kinds of oxygen species on oxides: surface adsorbed oxygen, which can easily be reduced and bulk lattice oxygen, which is active at relatively high temperatures only [37]. Research indicates that lattice oxygen of CeO₂ can selectively convert methane to CO and H₂ when the most reactive oxygen on the surface of oxygen carriers was removed [9,10,12]. In the CH₄–TPR tests for the Ce–Sm–O oxides, the surface oxygen species were mainly removed at low temperatures giving deep oxidation products, while syngas was mainly produced at higher temperatures [13]. Similar phenomena during the reaction between methane and solid oxides were also observed by Pantu et al. [21], Dai et al. [14,15], Wei et al. [17] and Nakayama et al. [18]. Fe₂O₃ was reported to participate in the complete oxidation of methane during the reduction from Fe₂O₃ to FeO, whereby the oxygen in FeO then selectively converts the methane to CO and H₂ [29,38]. As such, the formation of CO₂ and H₂O should be attributable to the consumption

Table 2

Average parameters for the selective oxidation of methane using Ce_{1-x}Fe_xO_{2-δ} oxygen carriers (x=0, 0.1, 0.2, 0.3, 0.4, and 0.5).

Oxygen carriers	CH ₄ conversion (%)	CO selectivity (%)	H ₂ selectivity (%)	n (H ₂):n (CO)
CeO ₂	24.2	92.3	87.3	1.89
Ce _{0.9} Fe _{0.1} O _{2-δ}	38.9	89.8	81.0	4.81
Ce _{0.8} Fe _{0.2} O _{2-δ}	52.5	86.6	74.0	2.11
Ce _{0.7} Fe _{0.3} O _{2-δ}	54.0	85.3	71.3	1.95
Ce _{0.6} Fe _{0.4} O _{2-δ}	62.6	85.1	68.9	2.61
Ce _{0.5} Fe _{0.5} O _{2-δ}	71.4	79.6	66.1	3.04

of the surface absorption oxygen and the $\text{Fe}^{3+} \rightarrow \text{Fe}^{2+}$ reduction, while the lattice oxygen in CeO_2 and FeO must be responsible for methane selective oxidation into CO and H_2 . For this reduction process, oxygen can be transported by the surface reaction and bulk ion conduction mechanism [12].

Several authors observed that the surface oxygen removed very rapidly during the reaction between methane and oxygen carriers [10,12–15]. Given this possibility, the first decline in conversion should be attributed to the rapid consumption of surface adsorbed oxygen. Any additional decline associated with the continued decline in pure CeO_2 would then be related to the depletion of available lattice oxygen. For the Ce–Fe samples, the later increase in conversion indicates enhanced reduction degree of materials. Shan et al. [35] observed an interaction between dispersed NiO species and the Ce–Ni solid solution, which strongly enhanced the catalytic activity necessary for methane combustion. We anticipated a similar situation with the dispersed Fe_2O_3 interacting with the solid solution to promote the surface reaction and oxygen mobility and thereby improving methane conversion.

Fig. 3(b) shows the effects of iron content in the oxygen carriers on the H_2/CO ratio during the reactions. The ratios for all the six samples were lower than 2.0 (1.5–1.8) at the very beginning of the reactions. Since the stoichiometric reaction of a CH_4 molecule with oxygen should yield a H_2/CO ratio of 2.0, ratios lower than 2.0 indicate the further oxidation of produced H_2 . With the reaction proceeding, the H_2/CO ratios increased rapidly to or over 2.0. Of the tested Ce–Fe samples, the $\text{Ce}_{0.7}\text{Fe}_{0.3}\text{O}_{2-\delta}$ sample maintained a H_2/CO ratio near the theoretical 2.0 value (i.e., 1.7–2.1) within the 12-min reaction. The ratios for the other Ce–Fe samples were significantly higher than 2.0 at the 12th minute (e.g., 5.6 for $\text{Ce}_{0.5}\text{Fe}_{0.5}\text{O}_{2-\delta}$ and 15.7 for $\text{Ce}_{0.9}\text{Fe}_{0.1}\text{O}_{2-\delta}$ samples), suggesting the presence of carbon deposition. This should be ascribed to the presence of a metallic iron due to the reduction of Fe_2O_3 , which can facilitate the methane decomposition [39]. It is predictable that the carbon deposition would be removed when the surface of oxygen carriers is rich in active-oxygen, and the high H_2/CO ratios (much higher than 2.0) therefore indicate relatively low oxygen concentration on the oxygen carriers with an inappropriate iron content. The H_2 -TPR (Fig. 2) results showed that the reducibility of Ce–Fe oxygen carriers was strongly affected by the iron content, and the $\text{Ce}_{0.7}\text{Fe}_{0.3}\text{O}_{2-\delta}$ sample revealed a high lattice oxygen activity because of the good interaction between free Fe species and Ce–Fe solid solution. This property would support the $\text{Ce}_{0.7}\text{Fe}_{0.3}\text{O}_{2-\delta}$ sample with sufficient active-oxygen for carbon removing during the reaction between methane and oxygen carriers.

3.4. Structure evolution during the reaction

To explore the reaction mechanism we investigated the structural evolution within the $\text{Ce}_{0.7}\text{Fe}_{0.3}\text{O}_{2-\delta}$ sample during its reaction with methane. After the reaction proceeded for several minutes at 850°C , the oxygen carriers were cooled down to room temperature under pure nitrogen. Figs. 4–6 show the XRD, Raman and XPS characterizations, respectively.

No new phase could be observed after the oxygen carrier was reduced by methane for 3 min, while the characteristic Fe_2O_3 peaks became much weaker in comparison with the fresh sample (Fig. 4). When the reaction time increased to 5 min, two new phases were detected (CeFeO_3 : $2\theta = 22.7, 25.4, 32.3, 38.8, 46.4, 57.7$ and 67.6° and metallic iron with a weak peak at 44.7°). It has been reported that cerium orthoferrite (CeFeO_3) could be prepared by the reaction $3\text{CeO}_2 + \text{Fe}_2\text{O}_3 + \text{Fe} \rightarrow 3\text{CeFeO}_3$ at $800\text{--}850^\circ\text{C}$ after a longtime (e.g., 48 h) of sintering under vacuum [40]. Our experiment revealed that a mixture (CeFeO_3 and Fe_2O_3) was obtained by heating the

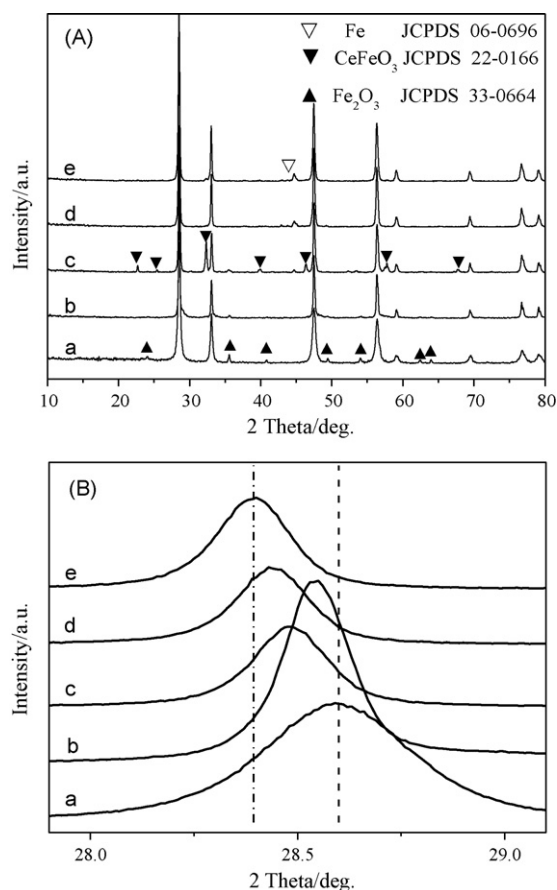


Fig. 4. XRD patterns (A with a scanning rate of $5^\circ/\text{min}$ and B with a scanning rate of $0.5^\circ/\text{min}$) of $\text{Ce}_{0.7}\text{Fe}_{0.3}\text{O}_{2-\delta}$ oxygen carriers after different treatments: (a) fresh $\text{Ce}_{0.7}\text{Fe}_{0.3}\text{O}_{2-\delta}$ sample, (b) after 3 min of reduction of the sample at 850°C , (c) after 5 min of reduction of the sample at 850°C , (d) after 7 min of reduction of the sample at 850°C and (e) after 12 min of reduction of the sample at 850°C .

$7\text{CeO}_2 + 3\text{Fe}$ mixture at 800°C in a reducing atmosphere for a much shorter time (less than 2 h, see Supplementary Fig. S1). Considering the better interfacial contact between cerium and iron species in the $\text{Ce}_{0.7}\text{Fe}_{0.3}\text{O}_{2-\delta}$ sample prepared by co-precipitation, the formation of CeFeO_3 should be attributed to a rapid solid–solid reaction between cerium oxide and reduced iron species. The sam-

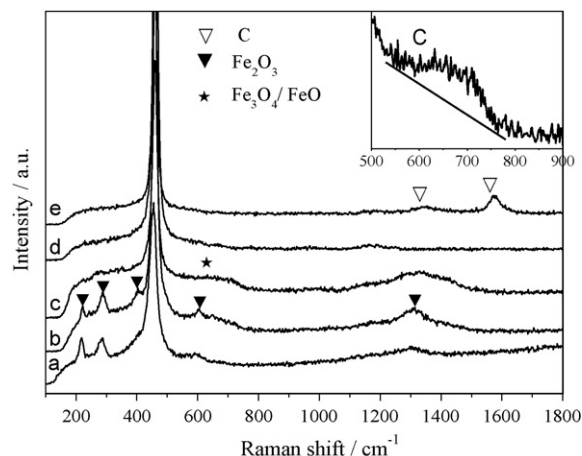


Fig. 5. Raman spectra of $\text{Ce}_{0.7}\text{Fe}_{0.3}\text{O}_{2-\delta}$ oxygen carriers after different treatments: (a) fresh sample, (b) after 3 min of reduction of the sample at 850°C , (c) after 5 min of reduction of the sample at 850°C , (d) after 7 min of reduction of the sample at 850°C and (e) after 12 min of reduction of sample at 850°C .

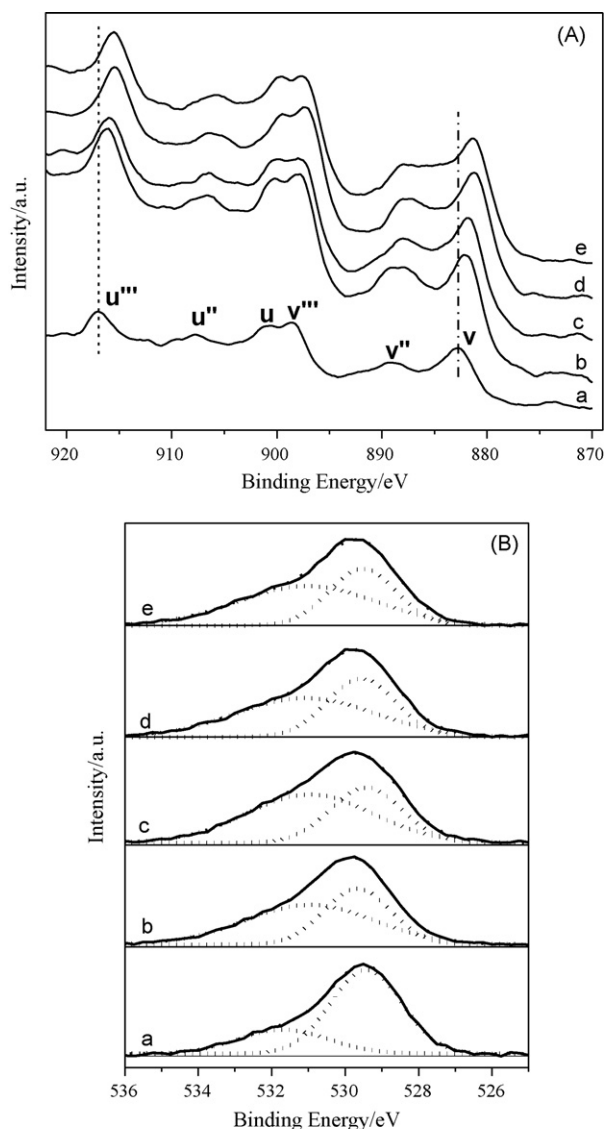


Fig. 6. XPS spectra of Ce 3d (A) and O 1s (B) for $\text{Ce}_{0.7}\text{Fe}_{0.3}\text{O}_{2-\delta}$ oxygen carriers after different treatments: (a) fresh sample, (b) after 3 min of reduction of the sample at 850 °C, (c) after 5 min of reduction of the sample at 850 °C, (d) after 7 min of reduction of the sample at 850 °C and (e) after 12 min of reduction of the sample at 850 °C.

ples reduced for 7 min and for 12 min only presented diffraction peaks for metallic iron and cerium oxide, which would indicate that all the iron oxide was reduced to metallic iron and the cerium oxides were the only oxygen source for methane oxidation at this stage.

Although no diffraction peaks for cerium suboxides (CeO_{2-x}) were observed in the entire set of five samples, obvious shifts of reflection around 28.5° corresponding to the (111) plane of fluorite-structured CeO_2 were detected by XRD measurement with a longer counting time per angular abscissa (Fig. 4B). The peak shift to lower 2θ position values originates from the lattice expansion of the fluorite structure owing to the presence of Ce^{3+} with a larger ionic dimension than Ce^{4+} (0.1012 nm vs. 0.097 nm) [34]. Since cerium suboxides (CeO_{2-x}) are easily re-oxidized to form stoichiometric CeO_2 [41], the appearance of reduced ceria suggests that re-oxidation of CeO_{2-x} at room temperature is slow under these conditions and that any further re-oxidation of the reduced samples is prevented by the formation of a thin layer of re-oxidized ceria [34].

Results from a Raman characterization (Fig. 5) provided more detailed surface information. The sample reduced for 3 min was similar to that for the fresh sample, which suggests that the weaker XRD peaks for Fe_2O_3 in the sample (Fig. 4A–b) should be attributed to enhanced dispersion of surface Fe_2O_3 rather than losses of Fe species during the reaction. After 5 min of reduction, the Raman bands towards Fe_2O_3 almost disappeared while a weak broad peak near 670 cm^{-1} and corresponding to the main Raman mode (A_{1g}) for FeO or Fe_3O_4 [42,43] was detected. After 7 min of reduction, no iron oxides could be observed. When the reaction time increased to 12 min, two weak bands indicating the formation of carbon were observed, one near 1340 cm^{-1} and the other near 1570 cm^{-1} [39]. This suggests the methane decomposition occurred due to the excessive consumption of lattice oxygen.

XPS was performed to investigate the surface chemical composition and valency/oxidation state changes upon methane treatments (Fig. 6). As reported, the Ce(IV) oxide is labeled with three pairs of $3d_{5/2}$ – $3d_{3/2}$ spin–orbit–split doublets (V – U , V'' – U'' and V''' – U''') for $4f^2$, $4f^1$, and $4f^0$ electron configurations, while Ce(III) oxide is characterized by two pairs of doublets (V° – U° , V' – U') representing the lower binding energy intensities of the $3d_{5/2}$ and $3d_{3/2}$ electrons for the $4f^1/4f^2$ configuration [44]. The Ce 3d spectrum for the fresh sample (Fig. 6A–a) containing six peaks at ca. 882.5, 889.0, 898.5, 900.8, 907.5 and 917.0 eV was clearly identified to be the Ce 3d spectrum for CeO_2 [44] with no evident signal for Ce^{3+} observed. This supports the observation that Ce^{3+} is absent in $\text{Ce}_{1-x}\text{Fe}_x\text{O}_2$ solid solution [24]. After the oxygen carrier was reduced with methane, the position of Ce 3d spectra gradually shifted to lower BE values, indicating an increase in Ce^{3+} [45].

The O 1s spectra (Fig. 6B) were fitted with two peaks at ca. 529.5 (main band) and 531.5 eV (shoulder band). The 529.5 eV peak is characteristic of the lattice oxygen in cerium oxide with the shoulder attributed to a defect oxide or surface hydroxyls associated with reduced Ce sites [28]. The signal decrease in the main band (ca. 529.5 eV) as well as the increase in the shoulder band (ca. 531.5 eV in Fig. 6B) suggests the lattice oxygen in the material was generally consumed along with the formation of surface defects during the reaction.

From XPS data, the Ce and Fe distributions seem to be non-homogeneous within the $\text{Ce}_{0.7}\text{Fe}_{0.3}\text{O}_{2-\delta}$ oxygen carrier. The fresh sample showed a Ce/Fe ratio of 3.44, well above the 2.33 value expected from nominal composition ($\text{Ce}/\text{Fe} = 7/3$). After the oxygen carrier was reduced by methane for 12 min, the surface Ce/Fe ratio increased to 6.47 and indicating that the sample surface must be enriched with Ce. Since the sample still presented XRD and Raman patterns similar to those for the fresh oxygen carrier (especially for Fe_2O_3 , see Supplementary Figs. S2 and S3) after 10 redox cycles (methane reduction/air re-oxidation), no further losses in Fe species should be expected with additional reaction time. This would suggest that Fe species might gradually migrate into or out of the inner core of the grain during the reduction/re-oxidation process.

To find out the effect of structural evolution on the redox property, H_2 –TPR measurements were performed over the four reduced $\text{Ce}_{0.7}\text{Fe}_{0.3}\text{O}_{2-\delta}$ oxygen carriers (Fig. 7). Based on the above analysis, the H_2 –TPR pattern for the fresh $\text{Ce}_{0.7}\text{Fe}_{0.3}\text{O}_{2-\delta}$ oxygen carrier was decomposed (Fig. 2) into three components at 490, 610, and 830 °C associated, respectively, with the reduction of Fe^{3+} located on the surface, the simultaneous reduction of Fe^{2+} and surface Ce^{4+} , and the reduction of bulk CeO_2 . The sample reduced for 3 min also had this shape, but the first peak shifted to a lower temperature (475 °C vs. 490 °C) while the second peak strengthened. On the other hand, it is also clear that the third peak assigned to the bulk reduction weakened and shifted to a higher temperature ($>900^\circ\text{C}$). This suggests that the ratio of surface/bulk reduction was higher than that of the fresh sample, evidencing the enhanced oxygen mobility within

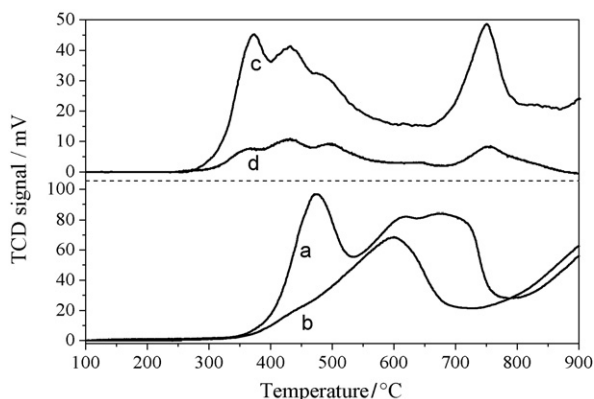


Fig. 7. H_2 -TPR profiles of $\text{Ce}_{0.7}\text{Fe}_{0.3}\text{O}_{2-\delta}$ oxygen carriers with different treatments: (a) after 3 min of reduction of the sample at 850°C , (b) after 5 min of reduction of the sample at 850°C , (c) after 7 min of reduction of the sample at 850°C and (d) after 12 min of reduction of the sample at 850°C .

the sample [33]. This can most probably be attributed to the promoted dispersion of surface iron species, which may affect the reduction kinetics of CeO_2 owing to the observed chemical interaction between cerium and iron species. When the reaction time increased to 5 min, a lower temperature shoulder was observed at ca. 440°C followed by a sharp peak centered at ca. 605°C . The slight shoulder corresponding to the reduction of surface Fe_2O_3 is in accord with the weak XRD and Raman figures towards the iron oxides on this sample (Figs. 4 and 5), while the sharp peak is most likely associated with the formation of CeFeO_3 .

A totally different and in some respects more interesting behavior was observed for the sample reduced by methane for 7 or 12 min. Both TPR profiles showed four peaks at ca. 370 , 430 , 480 and 750°C . The first three peaks at relatively lower temperatures (i.e., 370 , 430 and 480°C) should be related to surface reduction, with the high-temperature peak (750°C) originating from the reduction in bulk cerium oxide. The reduction temperatures for both surface and bulk oxygen were much lower than that required for the fresh oxygen carrier. Given the XRD and Raman tests results (Fig. 4A and Fig. 5), this promotion must be related to the presence of metallic iron on the surface of the cerium oxide. These phenomena indicate that both enhanced dispersion of surface iron species and the presence of metallic iron can strongly improve the reducibility of the cerium oxide.

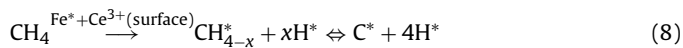
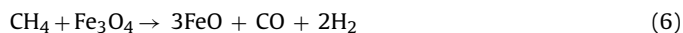
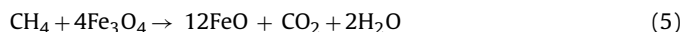
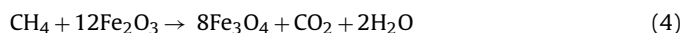
3.5. Reaction mechanism

Surface oxygen vacancies are generally proposed to participate in any number of chemical reactions catalyzed by metal oxides, and the exposed Ce^{3+} ions on CeO_2 are potentially potent surface sites for catalysis, because adsorbed gases or catalytic reaction intermediates can interact simultaneously with several Ce^{3+} ions [20]. For the reaction mechanism between methane and CeO_2 , Otsuka et al. [10] proposed that methane was activated on the reduced Ce^{3+} sites to form carbon intermediates and that CO was produced by the reaction of carbon with lattice oxygen of CeO_2 . They emphasized that neither the cleavage of the C–H bond in methane nor the diffusion of lattice oxygen could control the reaction rate, and the recombination or desorption of hydrogen should therefore be the rate-determining step in syngas formation. However, they also reported that the formation rate for H_2 and CO was strongly enhanced by the incorporation of ZrO_2 into CeO_2 , which would indicate that oxygen mobility played a likewise important role in the selective oxidation of methane [11]. In addition, Fathi et al. [12] observed that the reaction between methane and CeO_2 was strongly promoted by platinum or rhodium as well as sig-

nificant carbon deposition formation. They therefore suggested that methane decomposition on exposed Ce^{3+} sites was the rate-determining step for unpromoted CeO_2 , while carbon gasification by lattice oxygen of CeO_2 appeared to be the rate-determining step for the CeO_2 promoted by Pt or Rh. Based on these suggestions, the production of syngas using ceria-based oxygen carriers may be dominated by three key factors: (i) the activation of methane, (ii) the recombination of hydrogen atoms (or the desorption of H_2), and (iii) the oxygen mobility of materials.

The Ce–O–Fe interaction in Ce–Fe mixed oxides appear to play a significant role, since both single CeO_2 and Fe_2O_3 [30] show much lower activity. This interaction may occur by (i) formation of cubic ceria-like solid solution, which enhances oxygen mobility or (ii) close contact of exposed iron sites with solid solution, which plays a prominent role in the activation of reactants. This is similar to observations reported in [25,27]. The above results show that the reduction of surface Fe_2O_3 follows the path $\text{Fe}_2\text{O}_3 \rightarrow \text{Fe}_3\text{O}_4/\text{FeO} \rightarrow \text{Fe}$ (Figs. 4–6) accompanied by a rearrangement of the bulk and surface of the oxygen carrier (e.g., improved dispersion of surface Fe_2O_3 and the migration of exposed iron from surface to the bulk). Methane conversion and syngas selectivity increased during this process. Gemmi et al. [38] investigated the reduction of $\text{Fe}_2\text{O}_3/\text{CeO}_2$ solid ($n_{\text{Ce}}:n_{\text{Fe}} = 1:1$) by methane and proposed a reduction of CeO_2 in two steps, one when Fe_2O_3 is reduced to FeO and then other when the presence of metallic iron catalyzes enhance the cracking of methane, making the redox condition strongly reducing. However, attributing the enhancement of methane conversion only to the catalysis of reduced iron for methane decomposition based on the present results is somewhat problematic. In a study by Fukudaa et al. [46] the presence of the metallic iron was found to promote the desorption of H_2 while decreasing the desorption of CH_4 . The enhanced desorption of H_2 on Fe (1 0 0) in the presence of CO was also reported by Burke and Madix [47]. The XPS analysis (Fig. 6) shows that the amount of Ce^{3+} ions increased and the Fe species might gradually migrated into the inner core of the grain during the reduction process. The TPR presented in Fig. 7 shows that the reducibility of the Ce–Fe oxygen carrier was strongly improved by the reduction treatment, which indicates that oxygen in the Ce–Fe solid solution became more active due to the change of the surface properties (e.g., the presence of metallic iron sites, the increase of the surface Ce^{3+} and the migration of exposed iron from surface to the bulk). Given these findings, we should expect three key factors (the activation of methane, the desorption of H_2 , and the oxygen mobility of materials) to be enhanced by the presence of surface reduced species (i.e., metallic iron and Ce^{3+}).

The reactions between methane and $\text{Ce}_{0.7}\text{Fe}_{0.3}\text{O}_{2-\delta}$ can be proposed as follows:



The surface Fe_2O_3 is first reduced by methane (accompanied by the reduction of surface oxygen on mixed oxides) to produce CO_2 and H_2O , followed by the activation of methane on the reduced iron or cerium sites (Fe^* or Ce^{3+}) to create hydrogen atoms and carbon.

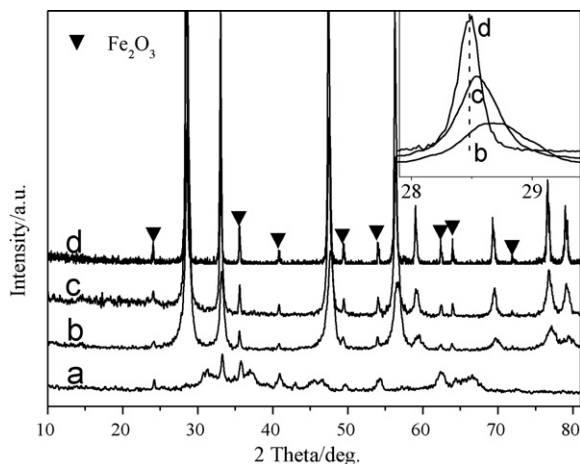


Fig. 8. XRD patterns of different oxygen carriers: (a) $\text{Fe}_2\text{O}_3/\text{Al}_2\text{O}_3$ sample prepared by co-precipitation, (b) $\text{Ce}_{0.7}\text{Fe}_{0.3}\text{O}_{2-\delta}$ sample prepared hydrothermally, (c) $\text{Ce}_{0.7}\text{Fe}_{0.3}\text{O}_{2-\delta}$ sample prepared by co-precipitation and (d) $\text{Ce}_{0.7}\text{Fe}_{0.3}\text{O}_{2-\delta}$ sample prepared by solid phase synthesis.

The hydrogen atoms recombine in pairs to molecules on the iron sites while the carbon is selectively oxidized to CO by the activated lattice oxygen ($\text{O}_{\text{Latt.}}^*$) releasing from the cerium oxides [48]. The interaction between the well-dispersed iron species and the lattice oxygen in the Ce–Fe solid solution (with good oxygen mobility) then promotes the formation rate of synthesis gas.

Based on these collective findings, it appears that both the dispersion of surface iron sites and the formation of a solid solution can affect the oxidation rate of methane. To understand the roles (and interactions) of the two species, a series of oxygen carriers with different Fe_2O_3 dispersion and/or iron dopant content were prepared and their catalytic performance in the selective oxidation of methane was compared.

3.6. The roles of free Fe_2O_3 and Ce–Fe solid solution

The XRD patterns for $\text{Fe}_2\text{O}_3/\text{Al}_2\text{O}_3$ and the three $\text{Ce}_{0.7}\text{Fe}_{0.3}\text{O}_{2-\delta}$ samples prepared by different methods (hydrothermal method, co-precipitation method and solid phase synthesis) are plotted in Fig. 8. The Al_2O_3 feature was not observed clearly in the $\text{Fe}_2\text{O}_3/\text{Al}_2\text{O}_3$ sample suggesting that this phase displayed poor crystallinity or small crystal size. Also the characteristic peaks towards Fe_2O_3 were very weak and broad, which indicated that Fe_2O_3 particles were well dispersed on the surface of an Al_2O_3 support. By contrast, the solid phase synthesis sample revealed the strongest peaks among the four oxygen carriers suggesting the largest crystal size. The lattice parameter for CeO_2 in this sample was very similar to that for pure CeO_2 (0.5412 nm vs. 0.5413 nm), indicating no Ce–Fe solid solution formation. The hydrothermal sample also presented two phases of CeO_2 and $\alpha\text{-Fe}_2\text{O}_3$, and the characteristic peaks for both species were much weaker and wider than those for the other two Ce–Fe samples (co-precipitation and solid phase synthesis samples). The crystallite sizes of Fe_2O_3 (14 nm) and CeO_2 (12 nm), calculated by the Scherrer equation, were much smaller than that for the co-precipitation sample (33 and 19 nm for Fe_2O_3 and CeO_2 particles, respectively). The contraction in the CeO_2 cell parameter (0.5384 nm for the hydrothermal sample vs. 0.5413/0.5395 nm for pure CeO_2 /co-precipitation $\text{Ce}_{0.7}\text{Fe}_{0.3}\text{O}_{2-\delta}$ sample) as well as the shift in the 2θ position (see the insert in Fig. 8) suggests more iron species was incorporated into the CeO_2 lattice hydrothermally.

Raman analyses are shown in Fig. 9. The iron oxides were hematite structures with five weak bands at approximately 220, 285, 404, 592 and 1298 cm^{-1} [25,42]. Almost no Raman features of

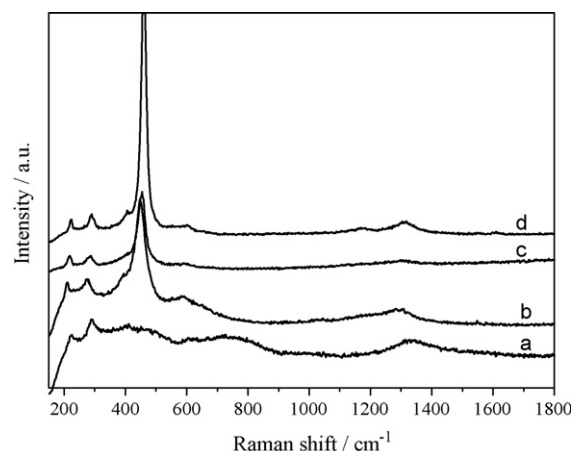


Fig. 9. Raman spectra of different oxygen carriers: (a) $\text{Fe}_2\text{O}_3/\text{Al}_2\text{O}_3$ sample prepared by co-precipitation, (b) $\text{Ce}_{0.7}\text{Fe}_{0.3}\text{O}_{2-\delta}$ prepared hydrothermally, (c) $\text{Ce}_{0.7}\text{Fe}_{0.3}\text{O}_{2-\delta}$ prepared by co-precipitation and (d) $\text{Ce}_{0.7}\text{Fe}_{0.3}\text{O}_{2-\delta}$ prepared by solid phase synthesis.

Al_2O_3 could be observed on $\text{Fe}_2\text{O}_3/\text{Al}_2\text{O}_3$ sample. This may be due to the poor crystallinity of Al_2O_3 powders and weak Raman sensitivity for aluminum oxides [49]. In the case of the Ce–Fe samples, they all revealed a prominent band at around 460 cm^{-1} owing to F_{2g} Raman active mode in metal dioxides with fluorite-like structure [25]. Raman spectra of the fluorite-type oxide structures are dominated by oxygen lattice vibrations and are sensitive to the crystalline symmetry [33]. Note that both the full width at half maximum (FWHM) of Raman bands at ca. 460 cm^{-1} and degree of the red shift of this peak for different oxygen carriers followed the order: hydrothermal sample > co-precipitation sample > solid phase synthesis sample. The widening of the ceria main line is related either to a decrease of ceria crystallite size or to the defects such as oxygen vacancies [50]. The red shift of the ceria band is reported to be characteristic of materials with enhanced oxygen mobility thereby signaling the formation of a solid solution [33]. This suggests that the hydrothermal $\text{Ce}_{0.7}\text{Fe}_{0.3}\text{O}_{2-\delta}$ sample had the most solid solution content and the smallest grains among the three Ce–Fe samples as suggested in the earlier XRD analyses.

Fig. 10 shows the typical kinetic curves for CH_4 conversion, CO and H_2 selectivity, and H_2/CO ratio for the reaction between $\text{Fe}_2\text{O}_3/\text{Al}_2\text{O}_3$ and methane at 850°C . The methane conversion declined rapidly from a relatively high level (about 57%) to the bottom within the first 4 min and then skyrocketed to a steady state (over 90%). The H_2/CO ratio maintained at around 2.0 during the decreasing stage for methane conversion, but it increased sharply (much larger than 2.0) as the conversion continued. The first decline

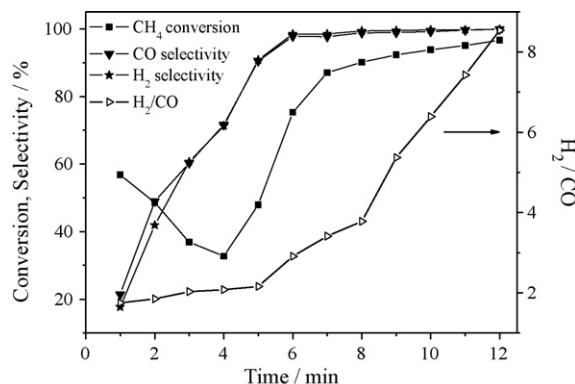


Fig. 10. Results from the reaction of methane with $\text{Fe}_2\text{O}_3/\text{Al}_2\text{O}_3$ oxygen carrier at 850°C .

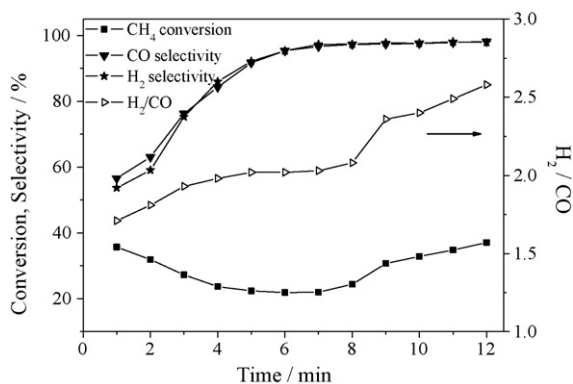


Fig. 11. Results from the reaction of methane with $\text{Ce}_{0.7}\text{Fe}_{0.3}\text{O}_{2-\delta}$ oxygen carrier, prepared by solid phase synthesis at 850°C .

in methane conversion can be attributed to the consumption of the oxygen in Fe_2O_3 , while the succeeding increase would be due to the methane decomposition. Although CO and H_2 selectivity increased quickly with reaction time, it presented a low value (about 20%) at the very beginning, which suggests that it is the surface or near-surface lattice oxygen of Fe_2O_3 ($\text{Fe}_2\text{O}_3 \rightarrow \text{Fe}_3\text{O}_4/\text{FeO}$) that converts the methane to CO_2 and H_2O while the deep oxygen contributes to the generation of CO and H_2 , as proposed in Eqs. (4)–(7).

Fig. 11 shows the test results for the reaction between methane and $\text{Ce}_{0.7}\text{Fe}_{0.3}\text{O}_{2-\delta}$ prepared by solid phase synthesis. The methane conversion was much lower than that of the co-precipitation sample (the average conversion for the co-precipitation sample was 54.0%, while it was just 25.8% for the solid phase synthesis sample). By contrary, the CO and H_2 selectivity showed a better feature, which started from a higher level (higher than 53%) and increased rapidly with the reaction proceeding. Given the XRD (Fig. 8) and Raman (Fig. 9) results, it appears the lower methane conversion should be related to the lack of solid solution with poor oxygen mobility. The higher selectivity, then, would result from the serious sintering of CeO_2 and Fe_2O_3 particles, which may result in a decrease in absorbed oxygen content. Interestingly, the H_2/CO ratio ranged from 1.71 to 2.58 with the average ratio of 1.97 through the 12 min test, which would indicate that CeO_2 might still be interacting with Fe_2O_3 to produce synthesis gas in the absence of Ce–Fe solid solution.

The $\text{Ce}_{0.7}\text{Fe}_{0.3}\text{O}_{2-\delta}$ oxygen carrier prepared hydrothermally was the most active sample for methane oxidation (Fig. 12). Methane conversion dropped from a high level of 89.2% to a low of 60.5% in 1 min and then rose rapidly above 81%. As described earlier, the first decline can be attributed to the rapid consumption of adsorption oxygen while the following increase can be assigned to the increase

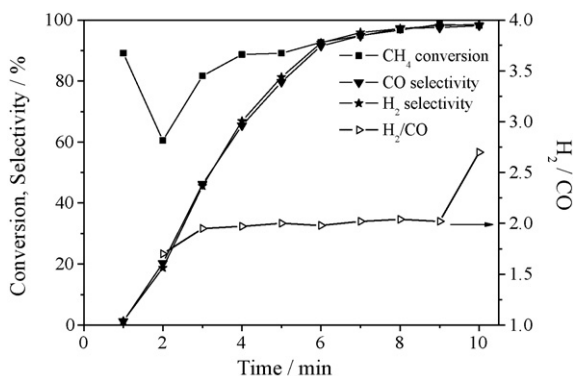


Fig. 12. Results from the reaction of methane with $\text{Ce}_{0.7}\text{Fe}_{0.3}\text{O}_{2-\delta}$ oxygen carrier, prepared by hydrothermal method at 850°C .

in active sites (reduced iron species). By contrast, CO and H_2 selectivity was rather low (less than 2%) at first before increasing rapidly with reaction time. Since the hydrothermal sample presented poor crystallinity, there may be more adsorption oxygen on the surface resulting in more CO_2 and H_2O in the preliminary stage. Of note, methane conversion and its rate of increase were much higher than that for the other two Ce–Fe samples. The H_2/CO ratio was also kept at around 2.0 (1.7–2.02) for 9 min, which was shorter than that for the co-precipitation or solid phase synthesis samples (12 min). These indicate a higher syngas formation rate resulting from the use of the hydrothermal oxygen carrier. The foregoing analysis suggests that synthesis gas is produced in two steps: (i) the decomposition of methane and (ii) the selective oxidation of carbon deposition. Further, the increased performance in methane selective oxidation using the hydrothermal oxygen carrier may be ascribed to two factors: (i) better dispersion of surface Fe_2O_3 and (ii) more Ce–Fe solid solution formation (with higher oxygen mobility), which promotes steps one and two, respectively.

3.7. Successive redox cycle performance test

3.7.1. Successive redox cycle performance

The hydrothermally prepared $\text{Ce}_{0.7}\text{Fe}_{0.3}\text{O}_{2-\delta}$ oxygen carrier was submitted to alternating reducing/endothermic and oxidizing/exothermic reactions to examine any successive production of syngas. The experiments were performed in a fixed-bed reactor at 850°C with flow rates of 10 and 60 mL/min for methane and pressed air, respectively. The reducing and oxidizing steps were separated by 15 min N_2 purge (80 mL/min). Syngas was generated continuously for 25 redox cycles (Fig. 13).

Similar trends towards CH_4 conversion, CO and H_2 selectivity, and the H_2/CO ratio were observed for each cycle when compared with the fresh sample (Fig. 12) and indicating the high reproducibility of the reducing sequences. Note that the initial methane conversion (at the first minute) slightly declined after several cycles (e.g., 89% for the fresh sample decreased to ca. 65% after 15 and more cycles), and the CO and H_2 selectivity increased mildly. Li et al. [51] reported that when reduced $\text{La}_{0.8}\text{Sr}_{0.2}\text{FeO}_3$ oxygen carriers were re-oxidized by air, the partially recovered samples showed a higher syngas selectivity. They therefore proposed that the lattice oxygen related to the formation of CO and H_2 was preferentially recovered. Dai et al. [14] investigated the redox reactions between LaFeO_3 and methane/oxygen and proposed that oxygen species (lattice oxygen) for the CO formation were easily recovered, while the reactive oxygen species (adsorbed oxygen) for the CO_2 formation were only minimally restored. As will be discussed next in the context, the H_2 -TPR profiles of the recycled $\text{Ce}_{0.7}\text{Fe}_{0.3}\text{O}_{2-\delta}$ sample (Fig. 16) shows that the characteristic peak due to the surface reduction (surface oxygen consumption) of the fresh materials almost disappeared after redox cycling, and the high-temperature peak (lattice oxygen consumption) was remarkably enhanced relative to that of the fresh samples. The decrease in methane conversion and the increase of syngas selectivity in Fig. 13, therefore, should be due to the decline in the surface oxygen species and the enhancement in the lattice oxygen content during the redox process.

3.7.2. Evolution of oxygen carrier after successive redox cycles

XRD and Raman measurements were used to investigate the structural evolution of the oxygen carrier after 25 successive redox cycles (Figs. 14 and 15, respectively). H_2 -TPR measurement was performed to probe the redox property of the Ce–Fe oxygen carrier during the successive hydrogen production (Fig. 16).

Fig. 14 shows that the CeO_2 peaks narrowed following redox treatments, which suggests an increase in crystal size. By contrast, the diffraction peaks of Fe_2O_3 became much weaker and broader, and the positions of the main peaks for CeO_2 shifted

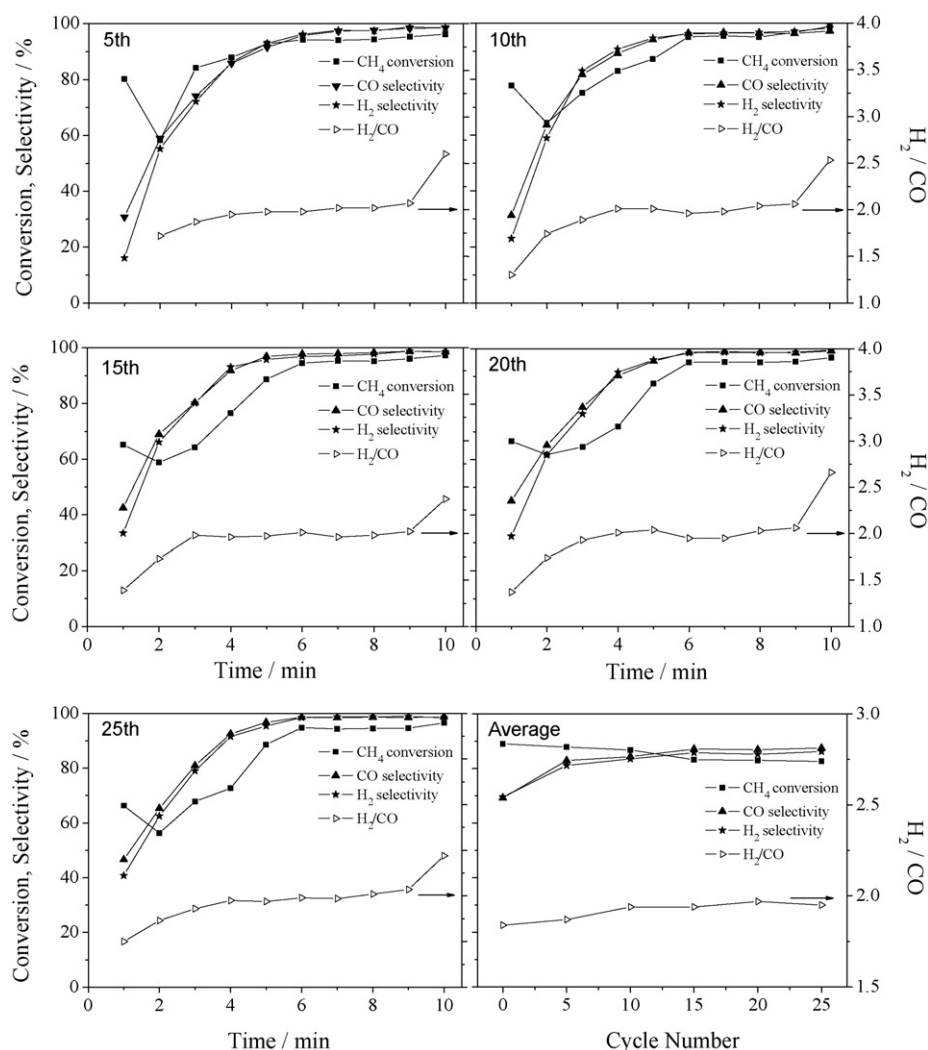


Fig. 13. The effect of redox cycle number on the selective oxidation of methane using $\text{Ce}_{0.7}\text{Fe}_{0.3}\text{O}_{2-\delta}$ oxygen carrier, prepared by hydrothermal method at 850°C .

slightly to higher values, which suggests that the surface Fe_2O_3 particles tended to be smaller and that the dopant content of iron ions increased after successive cycles at high temperature.

The Raman characterization presented in Fig. 15 supports the XRD results. Both the fresh and cyclic samples presented two

phases of CeO_2 and Fe_2O_3 . The narrowed band at ca. 450 cm^{-1} (the sign of fluorite-type structure of CeO_2) indicates the sintering of ceria while the red shift in the peak confirms increased solid solution formation after cycling. Unlike the XRD patterns (Fig. 14), there was no obvious weakening towards the intensity of characteristic

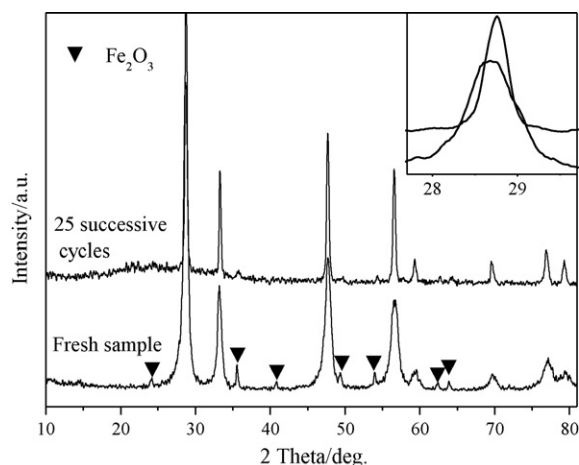


Fig. 14. Comparison of XRD patterns over fresh $\text{Ce}_{0.7}\text{Fe}_{0.3}\text{O}_{2-\delta}$ oxygen carrier and after 25 successive redox cycles.

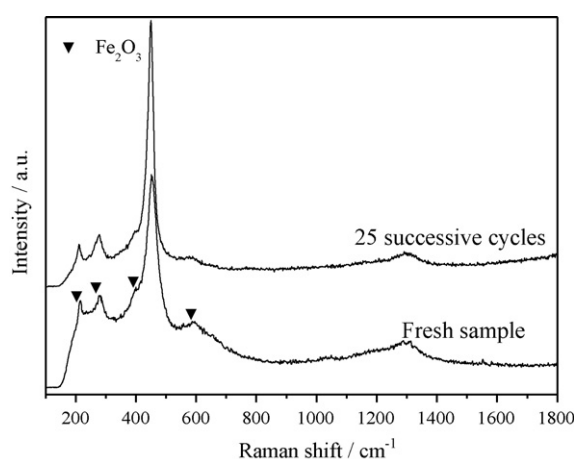


Fig. 15. Comparison of Raman spectra over fresh $\text{Ce}_{0.7}\text{Fe}_{0.3}\text{O}_{2-\delta}$ oxygen carrier and after 25 successive redox cycles.

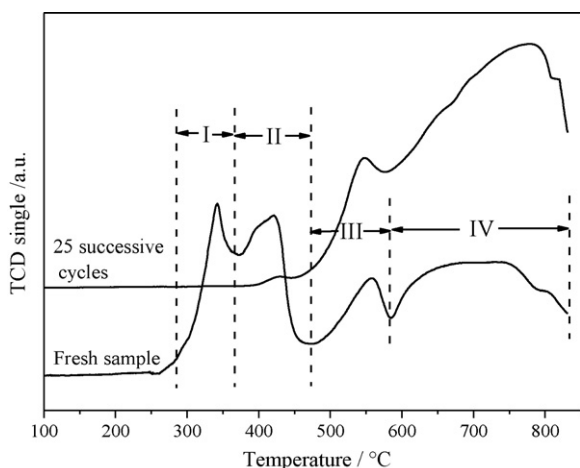


Fig. 16. Comparison of H_2 -TPR patterns over fresh $\text{Ce}_{0.7}\text{Fe}_{0.3}\text{O}_{2-\delta}$ oxygen carrier and after 25 successive redox cycles.

Fe_2O_3 peaks for the sample after 25 cycles. This verifies that the degradation of XRD peaks for Fe_2O_3 phase is due to the better dispersion of surface Fe_2O_3 particles rather than the losses of iron species.

The H_2 -TPR profile of the $\text{Ce}_{0.7}\text{Fe}_{0.3}\text{O}_{2-\delta}$ after 25 successive redox cycles was shown in Fig. 16, where it was compared with the corresponding TPR curve of the fresh sample. The TPR patterns of fresh $\text{Ce}_{0.7}\text{Fe}_{0.3}\text{O}_{2-\delta}$ sample can be divided in four temperature regions: region I (260–360°C), region II (360–470°C), region III (470–600°C), and region IV (600–830°C). To directly and accurately identify the attribution of each peak, additional experiments with the hydrothermally prepared CeO_2 and Fe_2O_3 were performed (see Supplementary Fig. S4). The TPR profile of CeO_2 shows two obvious peaks at ca. 520 and 894°C associated with the surface and bulk reduction of CeO_2 , respectively [34]. For the single Fe_2O_3 sample, two strong peaks were observed as well. The low-temperature peak at ca. 425°C can be assigned to the reduction of Fe_2O_3 to Fe_3O_4 and the high-temperature peak at ca. 745°C is supposed to be attributable to the reduction of Fe_3O_4 to Fe [32]. According to the reduction behavior of the single oxides, the regions I and II for the TPR patterns of the fresh $\text{Ce}_{0.7}\text{Fe}_{0.3}\text{O}_{2-\delta}$ sample should be related to the reduction of surface Fe_2O_3 and of the shell of CeO_2 , respectively. The small peak in the region III was assigned to the bulk reduction of iron oxides, while the broad band in the high-temperature region (region IV) indicated the removal of bulk oxygen in ceria. Dramatic changes occurred in the TPR behavior after redox treatment. There are two points which deserve to be highlighted: (i) the characteristic peak in TPR profiles due to the surface reduction (surface oxygen consumption) of the fresh materials almost disappeared after 25 successive redox cycles at 850°C; (ii) the recycled sample showed marked enhancement of the high-temperature ($T > 500^\circ\text{C}$) reducibility (lattice oxygen consumption) relative to that of the fresh samples. As established above, the surface absorbed oxygen in oxygen carriers is responsible for the complete oxidation of methane, while lattice oxygen can selectively convert methane into CO and H_2 . Therefore, the decrease in the surface oxygen species and the increase in the lattice oxygen content in the Ce–Fe oxygen carrier should be responsible for the improvement of the syngas selectivity during redox cycling, as observed in Fig. 13.

Generally, the thermal redox treatment at high temperatures ($T > 650^\circ\text{C}$) strongly modified the surface or bulk properties (e.g., lowering the specific surface area or causing the structural evolution) of CeO_2 -based materials, which could destroy the low-temperature reducibility of materials [34,52]. XRD and

Raman measurements (Figs. 14 and 15) show an obvious crystallite growth of CeO_2 phase for the recycled sample, and the BET characterization reveals that the specific surface area dropped from 41.6 to 4.7 m^2g^{-1} after 25 successive redox cycles. These phenomena should be responsible for the observed decline in low-temperature reducibility after redox treatment. It has been reported that the reduction behavior of the bulk lattice oxygen in Fe_2O_3 – $\text{Ce}_{0.5}\text{Zr}_{0.5}\text{O}_2$ oxides was enhanced when it was subjected to a repetitive reduction/oxidation cycle [53]. Atribak and co-workers [33] observed that the TPR profile of the aged $\text{Ce}_{0.76}\text{Zr}_{0.24}\text{O}_2$ mixed oxides (thermal treatment at 1000°C for 3 h) showed an enhanced high-temperature band instead of two well-defined peaks. They proposed that the surface and bulk reduction occurred concurrently for this type of profile, because oxygen located within the bulk would come to the surface immediately as surface oxygen was consumed, indicating a relatively high lattice oxygen mobility. As noted above, the dispersion of surface iron species and the formation of the Ce–Fe solid solution were shown to affect the reduction kinetics of CeO_2 owing to the observed chemical interaction between cerium and iron species. XRD and Raman measurements (Figs. 14 and 15) show that, upon a repetitive reduction/oxidation step, the surface Fe_2O_3 particles tended to be smaller and the dopant content of iron ions increased, which may promote the generation of highly mobile lattice oxygen by enhancing the Ce–Fe interaction, contributing to the enhancement of the high-temperature reducibility for the sample after cycling. This property permits the recycled Ce–Fe oxygen carrier to own a relatively high activity and selectivity for methane selective oxidation, although the specific surface area drops to a very low value.

In summary, continuous redox cycles result in the sintering of CeO_2 , but also promote the dispersion of surface Fe_2O_3 and Ce–Fe solid solution formation. Although the sintering of CeO_2 is negative for the low-temperature reducibility of oxygen carrier, the interaction between dispersed Fe_2O_3 and Ce–Fe solid solution can strongly enhance the lattice oxygen activity at relatively high temperatures. The resulting improvement in surface Fe_2O_3 dispersion and increased dopant content may counteract the negative effect of the sintering of oxygen carrier on the methane selective oxidation, and thereby contributes to the relatively high activity, selectivity and stability of hydrothermal $\text{Ce}_{0.7}\text{Fe}_{0.3}\text{O}_{2-\delta}$ oxygen carrier for the successive syngas production.

4. Conclusions

The direct conversion of methane to syngas using the lattice oxygen of Ce–Fe mixed oxides was investigated. Two forms of Fe species existed in the $\text{Ce}_{1-x}\text{Fe}_x\text{O}_{2-\delta}$ oxygen carriers with x varying from 0.1 to 0.5: iron ions incorporated into CeO_2 lattice to form a solid solution and exposed surface Fe_2O_3 . $\text{Ce}_{0.7}\text{Fe}_{0.3}\text{O}_{2-\delta}$ sample with co-existence of solid solution and free Fe_2O_3 showed the best reducibility.

The chemical interaction between free Fe_2O_3 and the solid solution was observed during the oxidation of methane and the interaction was used to describe the reaction mechanism between methane and the Ce–Fe oxygen carriers. Surface Fe_2O_3 was first reduced to create sites for activating both reactants (methane and lattice oxygen in solid solution). The methane on these sites was activated to carbonaceous species and hydrogen and allowing the carbon deposition to be selectively oxidized to CO by activated oxygen. The methane activation rate was dominated by the dispersion of surface iron species while the CO formation rate was related to oxygen mobility.

Further investigation into the role of surface iron species and Ce–Fe solid solution indicated that improvement in the dispersion of surface Fe_2O_3 and in the formation of the solid solution could

enhance the syngas formation rate. Use of hydrothermally prepared $\text{Ce}_{0.7}\text{Fe}_{0.3}\text{O}_{2-\delta}$ as an oxygen carrier revealed this optimization by maintaining high activity and stability during successive stages of syngas generation by a repetitive redox method (methane reduction/air re-oxidation).

Acknowledgements

Financial support from the National Nature Science Foundation of China (Project Nos. 50574046 and 50774038), National Natural Science Foundation of Major Research Projects (No. 90610035) and the Natural Science Foundation of Yunnan Province (No. 2008E030M).

Appendix A. Supplementary data

Supplementary data associated with this article can be found, in the online version, at [doi:10.1016/j.apcatb.2010.04.018](https://doi.org/10.1016/j.apcatb.2010.04.018).

References

- [1] B.C. Enger, R. Løeng, A. Holmen, Appl. Catal. A 346 (2008) 1–27.
- [2] J.R. Rostrup-Nielsen, Catal. Rev. Sci. Eng. 46 (2004) 247–270.
- [3] S.S. Bharadwaj, L.D. Schmidt, Fuel Process. Technol. 42 (1995) 109–127.
- [4] D.J. Wilhelm, D.R. Simbeck, A.D. Karp, R.L. Dickenson, Fuel Process. Technol. 71 (2001) 139–148.
- [5] J.R. Rostrup-Nielsen, Catal. Today 71 (2002) 243–247.
- [6] M.P. Kohn, M.J. Castaldi, R.J. Farrauto, Appl. Catal. B 94 (2010) 125–133.
- [7] E.R. Stobbe, B.A. Boer, J.W. Geus, Catal. Today 47 (1999) 161–167.
- [8] F. Van Looij, J.C. Van Giezen, E.R. Stobbe, Catal. Today 21 (1994) 495–503.
- [9] K. Otsuka, T. Ushiyama, I. Yamanaka, Chem. Lett. 22 (1993) 1517–1520.
- [10] K. Otsuka, Y. Wang, E. Sunada, I. Yamanaka, J. Catal. 175 (1998) 152–160.
- [11] K. Otsuka, Y. Wang, M. Nakamura, Appl. Catal. A 183 (1999) 317–324.
- [12] M. Fathi, E. Bjorgum, T. Viig, O.A. Rokstad, Catal. Today 63 (2000) 489–497.
- [13] V.A. Sadykov, T.G. Kuznetsova, G.M. Alikina, Y.V. Frolova, A.I. Lukashevich, Y.V. Potapova, V.S. Muzykantov, V.A. Rogov, V.V. Kriventsov, D.I. Kochubei, E.M. Moroz, D.I. Zyuzin, V.I. Zaikovskii, V.N. Kolomiichuk, E.A. Paukshtis, E.B. Burgina, V.V. Zyryanov, N.F. Uvarov, S. Neophytides, E. Kemnitz, Catal. Today 93–95 (2004) 45–53.
- [14] X.P. Dai, R.J. Li, C.C. Yu, Z.P. Hao, J. Phys. Chem. B 110 (2006) 22525–22531.
- [15] X.P. Dai, Q. Wu, R.J. Li, C.C. Yu, Z.P. Hao, J. Phys. Chem. B 110 (2006) 25856–25862.
- [16] Y.G. Wei, H. Wang, F. He, X.Q. Ao, C.Y. Zhang, J. Nat. Gas Chem. 16 (2007) 6–11.
- [17] H.J. Wei, Y. Cao, W.J. Ji, C.T. Au, Catal. Commun. 9 (2008) 2509–2514.
- [18] O. Nakayama, N. Ikenaga, T. Miyake, E. Yagasaki, T. Suzuki, Catal. Today 138 (2008) 141–146.
- [19] A. Trovarelli, Catalysis by Ceria and Related Materials, Imperial College Press, London, 2002.
- [20] C.T. Campbell, C.H.F. Peden, Science 309 (2005) 713–714.
- [21] P. Pantu, K. Kim, G.R. Gavalas, Appl. Catal. A 193 (2000) 203–214.
- [22] P. Vidmar, P. Fornasiero, J. Kaspar, G. Gubitosa, M. Graziani, J. Catal. 171 (1997) 160–168.
- [23] Z.C. Kang, L. Eyring, J. Solid State Chem. 155 (2000) 129–137.
- [24] G.S. Li, R.L. Smith, H. Inomata, J. Am. Chem. Soc. 123 (2001) 11091–11092.
- [25] F.J. Pérez-Ionso, M.L. Granados, M. Ojeda, P. Terreros, S. Rojas, T. Herranz, J.L.G. Fierro, M. Gracia, J.R. Gancedo, Chem. Mater. 17 (2005) 2329–2339.
- [26] G. Neri, A. Pistone, C. Milone, S. Galvagno, Appl. Catal. B 38 (2002) 321–329.
- [27] E. Aneggi, C. de Leitenburg, G. Dolcetti, A. Trovarelli, Catal. Today 114 (2006) 40–47.
- [28] H.Z. Bao, X. Chen, J. Fang, Z.Q. Jiang, W.X. Huang, Catal. Lett. 125 (2008) 160–167.
- [29] S. Takenaka, K. Nomura, N. Hanaizumi, K. Otsuka, Appl. Catal. A 282 (2005) 333–341.
- [30] K.Z. Li, H. Wang, Y.G. Wei, M.C. Liu, J. Rare Earths 26 (2008) 245–249.
- [31] K.Z. Li, H. Wang, Y.G. Wei, M.C. Liu, J. Rare Earths 26 (2008) 705–710.
- [32] G. Magnacca, G. Cerrato, C. Morterra, M. Signoretto, F. Somma, F. Pinna, Chem. Mater. 15 (2003) 675–687.
- [33] I. Atribak, A. Bueno-López, A. García-García, J. Catal. 259 (2008) 123–132.
- [34] E. Rocchini, A. Trovarelli, J. Llorca, G.W. Graham, W.H. Weber, M. Maciejewski, A. Baiker, J. Catal. 194 (2000) 461–478.
- [35] W.J. Shan, M.F. Luo, P.L. Ying, W.J. Shen, C. Li, Appl. Catal. A 246 (2003) 1–9.
- [36] F. He, Y.G. Wei, H.B. Li, H. Wang, Energy Fuels 23 (2009) 2095–2102.
- [37] E.J. Baran, Catal. Today 8 (1990) 133–151.
- [38] M. Gemmi, M. Merlini, U. Cornaro, D. Ghislettib, G.J. Artioli, J. Appl. Crystallogr. 38 (2005) 353–360.
- [39] S. Takenaka, M. Serizawa, K. Otsuka, J. Catal. 222 (2004) 520–531.
- [40] M. Robbins, G.K. Wertheim, A. Menth, R.C. Sherwood, J. Phys. Chem. Solid 30 (1969) 1823–1825.
- [41] J. Káspár, P. Fornasiero, M. Graziani, Catal. Today 50 (1999) 285–298.
- [42] D.L.A. De Faria, S. Venâncio Silva, M.T. de Oliveira, J. Raman Spectrosc. 28 (1997) 873–878.
- [43] S. Tiwari, R.J. Choudhary, D.M. Phase, Thin Solid Films 517 (2009) 3253–3256.
- [44] D.K. Kim, K. Stöwe, F. Müller, W. Maier, J. Catal. 247 (2007) 101–111.
- [45] P.F. Zhu, J. Li, S.F. Zuo, R.X. Zhou, Appl. Surf. Sci. 255 (2008) 2903–2909.
- [46] S. Fukudaa, T. Hinoa, T. Yamashina, J. Nucl. Mater. 162–164 (1989) 997–1003.
- [47] M.L. Burke, R.J. Madix, Surf. Sci. 237 (1990) 20–34.
- [48] K.Z. Li, H. Wang, Y.G. Wei, D.X. Yan, J. Phys. Chem. C 113 (2009) 15288–15297.
- [49] A. Mortensen, D.H. Christensen, F.O. Nielsen, E. Pedersen, J. Raman Spectrosc. 22 (1991) 47–69.
- [50] L. Ilieva, G. Pantaleo, J.W. Sobczak, I. Ivanov, A.M. Venezia, D. Andreeva, Appl. Catal. B 76 (2007) 107–114.
- [51] R.J. Li, C.C. Yu, X.P. Dai, S.K. Shen, Chin. J. Catal. 23 (2002) 549–554.
- [52] W. Mista, M.A. Malecka, L. Kepinski, Appl. Catal. A 368 (2009) 71–78.
- [53] V. Galvita, K. Sundmacher, J. Mater. Sci. 42 (2007) 9300–9307.